

Manuscript version: Author's Accepted Manuscript

The version presented in WRAP is the author's accepted manuscript and may differ from the published version or Version of Record.

Persistent WRAP URL:

<http://wrap.warwick.ac.uk/148474>

How to cite:

Please refer to published version for the most recent bibliographic citation information. If a published version is known of, the repository item page linked to above, will contain details on accessing it.

Copyright and reuse:

The Warwick Research Archive Portal (WRAP) makes this work by researchers of the University of Warwick available open access under the following conditions.

© 2021 Elsevier. Licensed under the Creative Commons Attribution-NonCommercial-NoDerivatives 4.0 International <http://creativecommons.org/licenses/by-nc-nd/4.0/>.



Publisher's statement:

Please refer to the repository item page, publisher's statement section, for further information.

For more information, please contact the WRAP Team at: wrap@warwick.ac.uk.

1 **On the effect of anisotropy on the performance and**
2 **simulation of shrinking tubes used as energy absorbers for**
3 **railway vehicles**

4

5

6

7 C. Moreno ^a, J. Winnett ^b, T. Williams ^a

8

9 ^a *OLEO International, Grovelands, Longford Road, Exhall, Coventry, CV7 9EN, UK*

10 ^b *WMG, University of Warwick, Coventry, CV4 7AL, UK*

11 Corresponding Author:

12 Carlos Moreno

13 OLEO International, Grovelands, Longford Road, Exhall, Coventry, CV7 9NE, UK

14 Tel: (0) 2476 015151

15 e-mail: carlos.moreno@oleo.co.uk

16 **Abstract**

17 The standard BS EN 15227 requires accurate numerical modelling of railway vehicle
18 energy absorbers that must be correlated against experimental data. Although thin-
19 walled tubes can exhibit anisotropy, such numerical models have traditionally
20 included isotropic material properties. Thus, this work investigates whether
21 anisotropic material models may increase the accuracy of numerical models of
22 shrinking tube energy absorbers.

23 Tensile testing of extruded AW-6082 aluminium alloy shrinking tubes showed the
24 yield strength of the tubes was 10% lower in the hoop direction than in the
25 longitudinal direction. Further, to assess the effect of incorporating anisotropic
26 material behaviour in the numerical model, the tubes were compressed under quasi-
27 static conditions.

28 Numerical models of the shrinking tubes, including isotropic (von Mises yield
29 function) and anisotropic (Hill's quadratic yield function) material properties, were
30 compared to the experimental data. The isotropic numerical models overestimated
31 the steady-state reaction force, even without the inclusion of friction, indicating that
32 such models do not fulfil the requirements of the standard. Conversely,
33 incorporating anisotropic material models predicted a lower reaction force and
34 enabled the inclusion of energy dissipation by friction, by means of a coefficient of
35 friction $\mu = 0.03$. Although these results demonstrate the need to include anisotropy
36 in the numerical simulation, the friction value was lower than expected due to the
37 methodology of the material characterization and the accuracy of the anisotropic
38 model implemented.

39 Keywords: shrinking tubes, material anisotropy, finite element analysis, coefficient of
40 friction

1 Introduction

The requirements for energy absorbers for railway vehicles are defined across two European Standards: BS EN 12663 [1], which specifies the loads that energy absorbers may transmit to different railway vehicle structures; and BS EN 15227 [2], which specifies the required amount of energy that the energy absorber must dissipate for each type of railway vehicle.

The latter also defines that these elements must provide overriding protection, by providing a methodology for colliding train units to engage, even if vertical offset or vertical loads are present during the collision [2]. Finally, it states that energy absorbing devices and crumple zones must be tested, with the results of full-size testing calibrated against the numerical model of the device. Therefore, the ability to produce numerical models that predict the energy absorbers performance accurately is a must for the manufacturers of railway vehicle energy absorbers.

The use of collapsible cylindrical elements as energy absorbers was pioneered by Alexander in the 1960s [3]. Crash boxes and crumple tubes, such as those used profusely in the automotive sector, have also found application in the railway industry, such as the structure developed by Stadler Rail [4], the work by Pereira et al. [5] or the multi-cell design proposed by Seitzberger et al. [6] from SIEMENS rail. More recently, thin-walled energy absorbers have implemented multi-cell tubes, foam-filled tubes or functionally graded thickness (FGT) tubes [7] to achieve the requisite performance. These structures are all progressive buckling elements, with type II load-deflection properties as defined by Calladine and English [8], and tend to be incorporated into the railway vehicle structure.

One of the major limitations of progressive buckling tubes is the fluctuating nature of the reaction force. Despite improvements to the uniformity of this force by the introduction of

64 corrugated tubes or functionally graded thickness (FGT) tubes [7], there is a tendency in the
65 railway industry to use type I energy absorbers, for bolted-on elements such as centre
66 couplers or anticlimbers. Of these, the most popular belong to four types of collapse modes:
67 splitting tubes, cutting tubes, expansion tubes and shrinking tubes.

68 The collapse mechanism of splitting tubes was pioneered by Stronge et al. [9] in the 1980s,
69 with this type of energy absorber now used commercially [10]. By splitting square
70 aluminium tubes, it was determined that energy was dissipated by fracture of the tube, the
71 subsequent plastic deformation as curls formed, and friction due to interaction between the
72 tube and the die [9]. Furthermore, theoretical models have been used to predict the
73 reaction force. A thorough review of the cutting mechanism of plates and extrusions, and
74 analytical models of these cutting mechanisms was undertaken by Magliaro and Altenhof
75 [11].

76 The potential for cutting-style energy absorbers for railway vehicles has also been studied
77 [12] [13] and subsequently commercialized [14]. These are based on the principle that the
78 energy is absorbed by plastic deformation during the cutting of chips and tearing of the
79 metal tube, as well as by friction between the knives and tube [12]. The peak force can be
80 varied by altering the cutting depth and angle of the cutting knife, whilst aluminium tubes
81 provide a more stable reaction force.

82 However, the primary technologies used by dedicated manufacturers of railway energy
83 absorbers, such as Voith [15], Dellner [16], or Oleo International [17] are based on
84 expansion and shrinking tubes.

85 Expansion tubes refer to those energy absorbers where energy is dissipated by the plastic
86 deformation of a radially expanding tube, as a conical die is forced through the cavity of the

87 tube. Friction generated by the surfaces in contact also acts to dissipate energy. Whilst the
88 energy is dissipated using similar mechanisms, shrinking tubes energy absorbers force the
89 tube through a conical die ring to reduce the diameter of the tube. These two energy
90 absorption mechanisms exhibit obvious similarities in the way the tube deforms, with the
91 tube subjected to bending in the meridional direction, and circumferential stresses, albeit
92 tensile in the case of expansion tubes and compressive in the case of shrinking tubes.

93 Radial expansion of tubes has been investigated since the early 2000s [18] [19] [20]. One key
94 parameter affecting the failure mode is the length of the tube, with longer tubes
95 experiencing buckling whilst shorter ones fail by diffuse necking [18]. Numerous numerical
96 models have been developed to assess the strain fields, which demonstrate high correlation
97 against test data. These include those based on force balance of membranes [19], balance
98 of forces [21] [22], energy balance [23] [24] [25], circle grid analysis [26] [27] [28], and
99 eccentric compression [29], with consideration also made for shear effects [30]. Whilst
100 primarily based on expanding steel, models have also been developed for use with
101 aluminium [31]. The numerical models are highly dependent on the friction coefficient
102 implemented to ensure correlation, with μ values ranging from 0.02 to 0.30, depending on
103 model parameters. Once validated, such models can be used to understand deformation
104 mechanisms [32] and hence optimise structures for maximal specific energy absorption
105 (SEA) by considering the conical semi-angle, wall thickness and expansion ratio [33] [34].

106 Shrinking tubes have attracted somewhat less attention than expansion tubes in the context
107 of energy absorption. However, they demonstrate greater energy dissipation efficiency than
108 expansion tubes [35] [36]. As with those developed for expansion tube energy absorbers,
109 models can be used for optimisation of the tube and die parameters [35] [37], as well as to

define novel energy absorbers that combine shrinking and splitting for a significantly improved (60%) absorption capability [38].

The analytical models, as well as finite element (FE) models described all assume isotropic material behaviour, with isotropic yield criterion (either von Mises or Tresca). Furthermore, beyond yield, the material was assumed to be perfectly plastic or could be modelled using isotropic hardening. It is also worth noting that the value of the friction coefficient is determined by matching the test and numerical results. Remarkably, most researchers converged to similar values for the friction coefficients, with these summarised in Table 1. It can be noted that the friction coefficient ranges from $\mu = 0.02$ to 0.25, with modal values of $\mu = 0.05$ during expansion, with this increasing to 0.11 for shrinking tubes. The authors of the present study have previously observed [39] a friction coefficient value of $\mu = 0.05$ for shrinking tubes used as rail vehicles anti-climbers.

Table 1: Assessed coefficients of friction by different researchers and different tube deformation mechanisms, from physical experimentation and for a lubricated friction regime.

DEFORMATION MECHANISM	COEFFICIENT OF FRICTION	CONDITION	REF.
Expansion	0.10	Lubricated	[18]
Expansion	0.02	Lubricated	[20]
	0.20	Dry	
Shrinking	0.08	Lubricated	
	0.30	Dry	
Expansion	0.05	Coated	[29]
	0.10	Dry	
	0.25	Blasted	
Expansion	0.05	Lubricated	[33]
Expansion	0.06	Lubricated	[22]
Expansion	0.05	Lubricated	[31]
Inversion	0.05	Lubricated	[28]
Shrinking	0.14	Dry	[34]
Shrinking	0.10	Lubricated	[35]
Shrinking	0.08	Lubricated	[37]

It is worth noting that adjusting the friction coefficient within the simulation to match the test results to the model is only a valid approach if all other model parameters are accurate. Indeed, such adjustments may obscure the effect of the other parameters, such as the properties of the material used to manufacture the tubes, on the performance of the energy absorbers.

The effect of anisotropy in tubes has also been investigated. Inclusion of non-quadratic yield functions, such as Hosford and Karafillis-Boyce, [40] and advanced anisotropic models [41] offered a better prediction during finite element analysis of the failure of hydroformed aluminium tubes. Additionally, such models have been used to enhance the understanding of the effects of expanding tubes during compression beading [42] and the formability of thin-walled aluminium tubes through correlation with forming limit curves (FLC) and fracture forming lines (FFL) [43].

This suggests that the performance of expansion tubes used as energy absorbers may be affected by the anisotropic nature of the material. In particular, the reaction force of anisotropic expansion tubes may not be accurately predicted using traditional isotropic material models, thus failing to meet the requirements of BS EN 15227 [2].

Thus, the objective of this paper is to assess the effect of anisotropy on the performance and simulation of AW-6082 T6 aluminium alloy shrinking tubes used as energy absorbers for railway vehicles.

2 Experimental and Numerical Simulation Methodology

2.1 Experimental set-up

Quasi-static tests were performed using a Hounsell hydraulic press with a maximum load limit of 3000 kN and a maximum displacement of 450 mm, with the experimental setup shown in Figure 1. The reaction force was measured using a Tokyo Sokki Kenkyujo 2000 kN load cell (CLC-2MNA), whilst vertical displacement of the hydraulic actuator was measured using a wire potentiometer (PT101) with a range of 50 ". The specimens were supported by the load cell, while the load was applied quasi-statically onto the upper surface of the specimens at an approximate rate of 4 mm/s. The specimens were lubricated using anti-slip copper grease to reduce the possible variable response caused by friction. The lubricant was applied over the external surface of the deformation tube and the inner bore of the die ring.

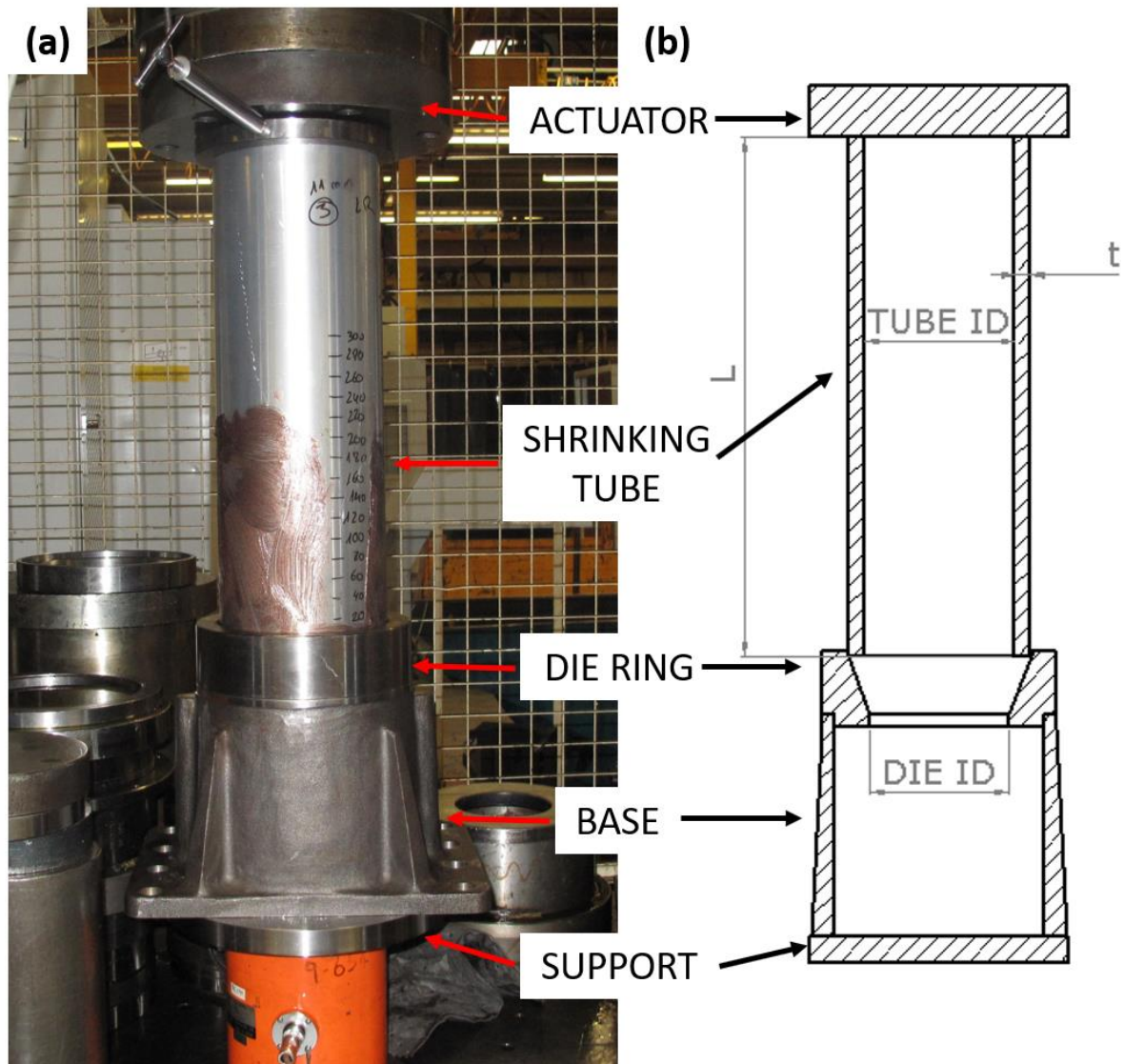


Figure 1: (a) Test rig and specimen assembly; (b) schematic diagram of the experimental setup.

The whole assembly comprised the supporting base, the shrinking die ring and the deforming tube. The experiments included testing of tubes manufactured by a direct extrusion process with three different wall thicknesses.

Three conical shrinking die rings with three different shrinking ratios were manufactured from 817M40 tool steel. Here, the nominal shrinking ratio of the deformation tube was defined as the ratio of the inner diameter of the die ring to outer diameter of the undeformed tube. In this manner, when the ratio of the ring inner diameter to the

168 undeformed tube outer diameter was 0.91, the shrinking ratio was defined as 9%. Likewise,
169 when the diameter ratios were 0.87 and 0.77, the shrinking ratios were defined as 13% and
170 23% respectively. For simplicity, these ratios are referred hereafter as R10, R15 and R25,
171 respectively. As observed elsewhere [35], the tubes do not conform to the shape of the ring
172 die and exhibit a gap between the reduced outer diameter of the tube and the inner
173 diameter of the die due to the bending rigidity of the wall of the tube. Thus, the actual
174 shrinking ratios are anticipated to be larger than the quoted nominal, due to the bending
175 rigidity of the inward bending tube.

176 The combination of three tube wall thicknesses and three die ring inner diameters produced
177 nine different test configurations. The specimens which were aimed at achieving forces
178 around 500 kN and which included the smallest wall thickness are referred as F050.
179 Likewise, the specimens which aimed to achieve around 1000 kN of force, which included
180 the middle wall thickness, are referred as F100. Finally, the specimens which aimed to
181 achieve around 1500 kN of force, which included the largest wall thickness, are referred as
182 F150. The nomenclature was completed with the shrinking ratios R10, R15 and R25. For
183 example, the test configuration including a tube aimed at achieving a force 500 kN and
184 including a shrinking ratio $R = 10\%$ shall be called F050R10, and the test configuration
185 including a tube aimed at reaching a force of 1500 kN and including a shrinking ratio $R = 15\%$
186 shall be called F150R15. The length of the first batch of specimens (those specimens labelled
187 "01" in Table 3) was $L = 500$ mm, with this decreased in the second batch to $L = 300$ mm (the
188 specimens labelled "02" in Table 3).

2.2 Material Properties

The deformation tubes were made of aluminium alloy AW-6082 T6, as per BS EN 573-3 [44]. The tubes were manufactured as direct extrusions, with material properties of the tubes determined through tensile tests undertaken in accordance with BS EN 6892-1:2009 [45]. Tensile tests were performed on material extracted along the longitudinal direction to the axis of the tube as well as along the transversal direction. Thus, testing on these two coupons, one for each direction, was aimed at capturing the different properties of the material along two major axes of symmetry: longitudinal and hoop directions. The small thickness of the wall prevented testing coupons in the other axis of symmetry, that is, along the radial orientation.

The material of the die ring, 817M40 tool steel, has minimum quoted values for yield strength $\sigma_y = 740$ MPa, ultimate strength $\sigma_u = 910$ MPa and elongation $e = 12.0\%$.

2.3 Constitutive Model

The reaction force in shrinking tubes is traditionally predicted using an isotropic material model for the tube material properties as stated in section 1, with an isotropic yield criterion. The yield criterion defines the yield surface, i.e. the threshold of a multiaxial stress state at which the material undergoes plastic deformation. The Von Mises yield criterion, shown in equation (1) where σ_y is the uniaxial yield strength, is the most commonly used for isotropic materials.

$$\frac{1}{2}[(\sigma_1 - \sigma_2)^2 + (\sigma_2 - \sigma_3)^2 + (\sigma_3 - \sigma_1)^2 + 6(\sigma_4^2 + \sigma_5^2 + \sigma_6^2)] = \sigma_y^2 \quad (1)$$

Herein, a material model based on the von Mises yield criterion was used with the numerical models to predict the reaction force of the shrinking tubes in the traditional

210 manner. However, this does not account for different material properties in the longitudinal
211 and hoop directions.

212 Assuming orthogonal symmetry, Hill [46] developed one of the first anisotropic yield
213 functions, often referred to as Hill'48 quadratic yield criterion. In the case of cylindrical
214 tubes, the principal axes of anisotropy correspond to the radial, circumferential and
215 longitudinal directions. The proposed function is of the form shown in equation (2), where F,
216 G, H, L, M, and N are the anisotropy parameters to be defined.

$H(\sigma_1 - \sigma_2)^2 + F(\sigma_2 - \sigma_3)^2 + G(\sigma_3 - \sigma_1)^2 + 2(N\sigma_4^2 + L\sigma_5^2 + M\sigma_6^2) = 1$	(2)
---	-----

217 The relationships between these parameters are as shown in equations (3) through (8)
218 where X, Y, Z are the tensile yield stresses in the principal anisotropic directions; and R, S, T
219 are the yield stresses in shear with respect to the same principal axes.

$\frac{1}{X^2} = G + H$	(3)
$\frac{1}{Y^2} = H + F$	(4)
$\frac{1}{Z^2} = F + G$	(5)
$L = \frac{1}{2R^2}$	(6)
$M = \frac{1}{2S^2}$	(7)
$N = \frac{1}{2T^2}$	(8)

220 In the case of rotational symmetry about the z axis, the relations (9) and (10) are also true.

$F = G$	(9)
$N = G + 2H$	(10)

221 Whilst there exists a wealth of more advanced anisotropic yield criteria [47], Hill'48 will be
222 used for the purposes of this investigation. This is due to the simplicity of the Hill'48
223 anisotropic yield criterion and its similarity to the well-known von Mises isotropic yield
224 criterion. Also, this model is readily available to implement within the finite element code of
225 choice, as detailed below.

The Hill'48 yield criterion requires 6 parameters in order to be fully defined. Due to the complexity of determining the material properties of the tube in the radial direction, it was assumed that the shrinking tube exhibits rotational symmetry, enabling the adoption of transverse isotropy. Under this assumption the anisotropic parameters F and G comply with equation (9). An additional simplification is that the shear yield stresses about the x and y axes are not affected by anisotropy. This assumption implies that the anisotropic parameters L and M would take the same values as in the isotropic conditions [47]. Therefore, the anisotropic parameters F (or G) and H need to be determined, requiring the tensile yield stresses in two directions, the longitudinal and hoop directions.

2.4 Finite Element Modelling

Shrinking tubes exhibit axisymmetrical deformation. Thus, and to reduce computational time, axisymmetric finite element models were built using the explicit finite element commercial software LS-DYNA and run using two Intel Xeon E5-2667 v3 processors with shared memory parallel processing (SMP). The model of the shrinking tube used to perform the force reaction prediction based on isotropic material properties, shown in Figure 2, comprised five different parts: the deformation tube (A), the die ring (B), the base (C), the stationary rigid base (D) and the driving rigid tube (E). Figure 2 (a) shows the initial mesh, whilst Figure 2 (b) shows the deformed shape. The base (C) and die (B) ring were fully constrained by a rigid section at the end of the base (D). The tube (A) was forced through the die ring (B) by means of a rigid section of the tube (E), which was given a constant speed (*BOUNDARY_PRESCRIBED_MOTION_RIGID). This section was allowed to move on the XY axisymmetric plane but constrained in the Z out-of-plane direction.

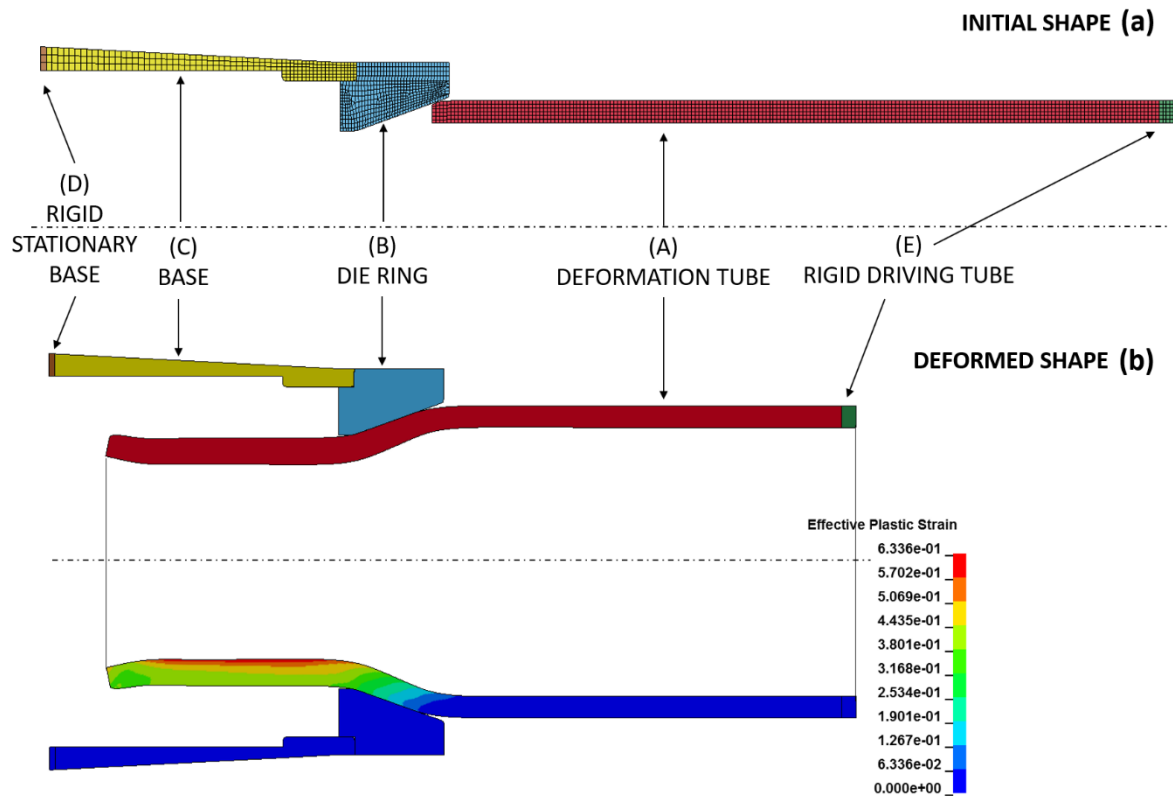


Figure 2: Axisymmetric numerical model of the shrinking tube.

The dedicated automatic penalty-based axisymmetric contact

*CONTACT_2D_AUTOMATIC_SURFACE_TO_SURFACE was used between the deformation tube and the die ring, parts (A) and (B), as described by the LS-DYNA manual [48]. Shell elements with element formulation 15 (2D axisymmetric solid elements) were included in the model. Four integration points were implemented to prevent hourglass modes. The LS-DYNA material model (*MAT_PIECEWISE_LINEAR_PLASTICITY) captures the material plasticity by introducing a monotonically increasing curve.

Tensile test samples are typically extracted from the longitudinal direction of the tube, as the wall thickness of most tubes makes it impracticable to extract tensile samples in the transverse direction. This approach was followed by several researchers quoted in the introduction [22] [31] [35] [37] [39]. Herein, data obtained from samples extracted from

both the longitudinal and transverse directions of the tube is implemented. The experimentally derived stress-strain curves were converted into true stress-true strain curves and imported into the material card of the deformation tube. In this manner, the tubes are assumed to be isotropic, with similar material properties in every direction. The material model included for the die ring was 817M40 steel, with mechanical properties as previously described.

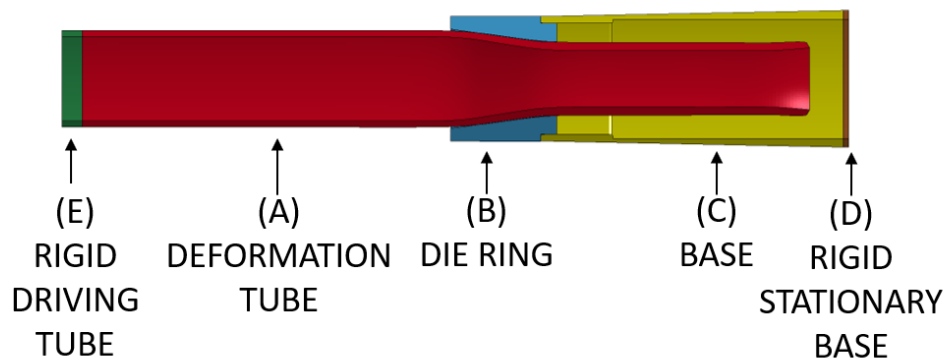
To assess the sensitivity of the model to element density, discretization through the wall thickness of the deformation tube of 6, 12 and 24 elements was evaluated. In accordance with other researchers [20] [22] [34], the tests were performed quasi-statically. Time scaling, which virtually increases the model speed, was used to reduce the run-time. However, this can introduce spurious inertial effects on the highly accelerated parts which do not represent the real behaviour of the tube. Thus, three different models were built using 6 elements through the wall thickness and with the speed of the base and die ring parts, parts (B) and (C), varied to 0.1, 1.0 and 10.0 m/s. The run-time was 1 hour 22 minutes, 24 minutes, and 3 minutes for the 0.1, 1.0, and 10.0 m/s models respectively. The final mesh density ranged between 2000 and 3000 elements.

To implement Hill'48 material model for solid elements, 3D numerical models were constructed. The selection of 3D models was motivated by the fact that LS-DYNA Hill'48 anisotropic material model is only implemented for solid elements. In the same manner as the axisymmetric model, the solid model comprised five different parts: the deformation tube (A), the die ring (B), the base (C), the stationary rigid base (D) and the driving rigid tube (E), as shown in Figure 3 (a). One-eighth of the shrinking tube was modelled to save computational time. Therefore, the model was made of a 45° solid of revolution around the

286 longitudinal axis of the tube, Figure 3 (b). The deformation tube part included 6 elements
287 through the wall thickness, which resulted in models with approximately 60000 elements.
288 Symmetric boundary conditions were applied on the faces shown, using local coordinate
289 systems. The LS-DYNA material model *MAT_HILL_3R_3D includes Hill'48 anisotropic
290 plasticity theory. The model is available for solid elements and accepts the dimensionless
291 anisotropic parameters F, G, H, L, M, N. The z axis must be used as the reference
292 (longitudinal) direction. The material model *MAT_HILL_3R_3D was included, together with
293 the experimentally determined anisotropic parameters.

294 The critical deformable parts, such as the deformation tube and the die ring, included at
295 least six elements through thickness, to accurately capture their deformation. To avoid
296 hourglassing, fully integrated hexahedral solids, element formulation 2, with a characteristic
297 length of 1-2 mm were used. An automatic penalty-based contact formulation was selected
298 for the areas in contact (*CONTACT_AUTOMATIC_SURFACE_TO_SURFACE).

(a) 3D MODEL



(b) SYMMETRIC BOUNDARY CONDITIONS (1/8 MODEL)

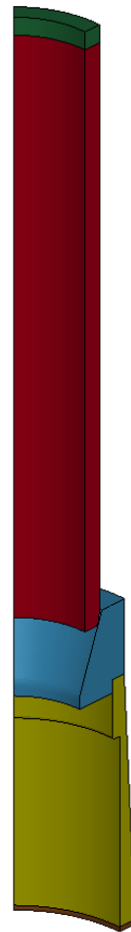
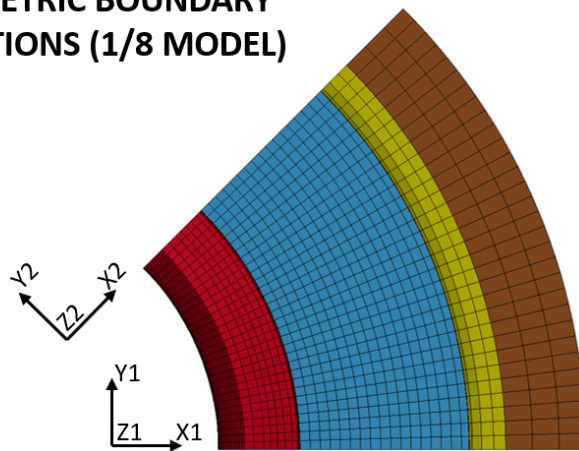


Figure 3: (a) 3D solid numerical model of the shrinking tube; and (b) symmetry boundary conditions.

3 Results

3.1 Material Properties

The engineering stress-strain curve of the two coupons is shown in Figure 4. The measured yield strengths were $\sigma_y = 327$ MPa and 293 MPa, whilst the ultimate strengths were $\sigma_u = 373$ MPa and 339 MPa, and the elongations were $e = 14.3\%$ and 13.7% , for the longitudinal and transversal coupons respectively. With an average yield stress ratio between the two curves of 0.90, the strength of the tube in the hoop direction was 10% weaker than in the longitudinal direction, indicating the quantifiable material anisotropy of the aluminium extrusions.

A simple power curve relation of the form $\sigma = K\epsilon^n$ was fitted to the data, resulting in parameters $K_{\text{long}} = 432.5$ MPa and $n_{\text{long}} = 0.0590$ for the axial coupon data; and $K_{\text{trans}} = 396.5$ MPa and $n_{\text{trans}} = 0.0606$ for the transversal coupon data.

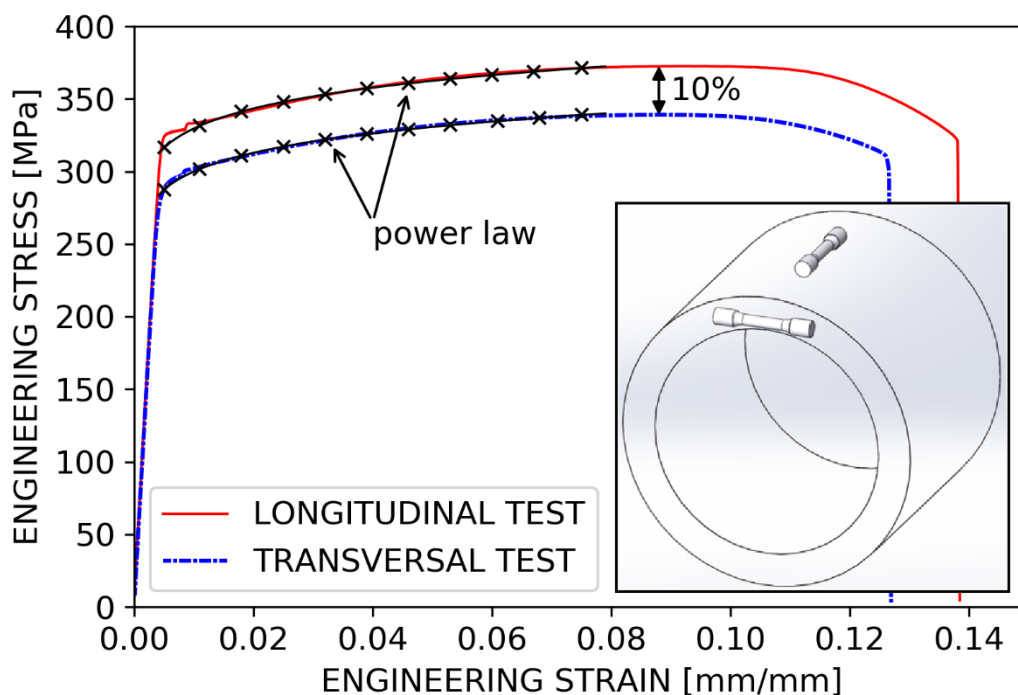


Figure 4: Engineering stress-strain properties of the longitudinal and transversal coupons from the AW-6082 T6 extruded tubes, from tensile test.

The tensile yield stresses were used with Equations (2) to (10) to determine the anisotropic parameters. The results were $F = G = 0.500/Z^2$, $H = 0.735/Z^2$ and $N = 1.970/Z^2$. In order to convert these to dimensionless parameters, the equations were pre-multiplied by Z^2 . The values of the anisotropic dimensionless parameters are shown in Table 2, together with their counterpart values for an isotropic material. Notice that the values of M and L have been assumed isotropic in both cases.

Table 2: Isotropic and anisotropic Hill'48 parameters for the AW-6082 T6 aluminium tubes.

	H	F	G	N	L	M
ISOTROPIC	0.500	0.500	0.500	1.500	1.500	1.500
ANISOTROPIC	0.735	0.500	0.500	1.970	1.500	1.500

3.2 Experimental Results

One specimen of each of the test configurations with a shrinking ratio of 10% was tested, test configurations F050R10, F100R10 and F150R10. Figure 5 shows the deformed shapes of these tubes after test once the undeformed ends for further testing had been removed, and the force-displacement properties of the three tubes. The steady-state force was 262.1, 514.9 and 721.1 kN for the F050R10, F100R10 and F150R10 samples respectively.

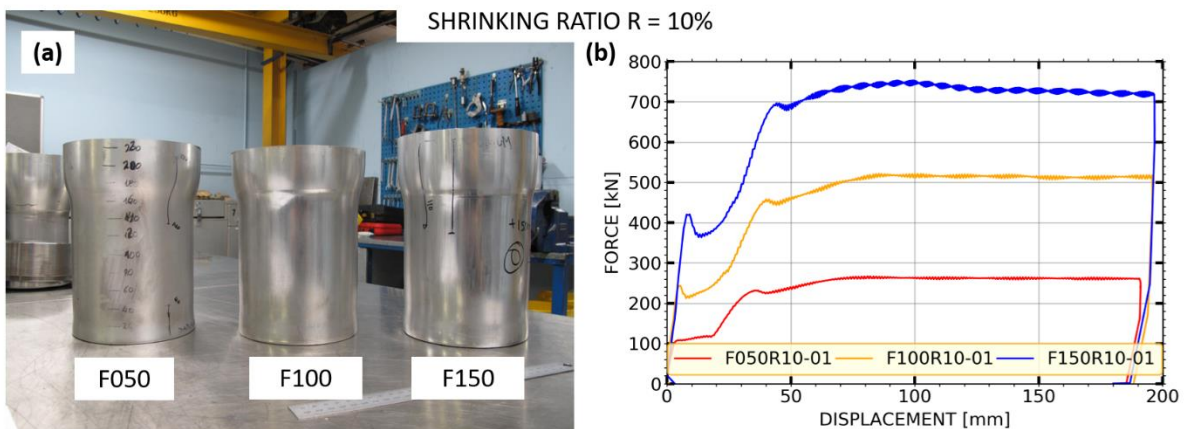


Figure 5: (a) Photograph of the shrinking tubes with shrinking ratio 10% after test; and (b) experimental force-displacement properties of the three specimens.

For the tubes with 15% shrinking ratio, F050R15, F100R15 and F150R15, specimens with 500 mm (-01) and 300 mm (-02) length of each configuration were tested, with the deformed shapes of these tubes after test and their force-displacement properties shown in Figure 6. The steady-state forces were 340.1, 596.4 and 868.7 kN for the F050R15-01, F100R15-01 and F150R15-01 samples respectively, with slightly increased values of 345.8, 596.7 and 914.7 kN for the shorter F050R15-02, F100R15-02 and F150R15-02 samples. Again, the undeformed ends of the tubes were cut and removed after testing, although the F150R15 specimen is shown prior to cutting. The force-displacement properties of the F150R15 with a 300 mm tube length (F150R15-02) were measured after a pre-deformation stage of 100 mm of stroke, and therefore the force response of the tube increases almost immediately to the steady-state force of the tube. It can be observed that, in this latter case, the force properties exhibited a marked peak, approximately 1000 kN, followed by a gentle settling towards the steady state force.

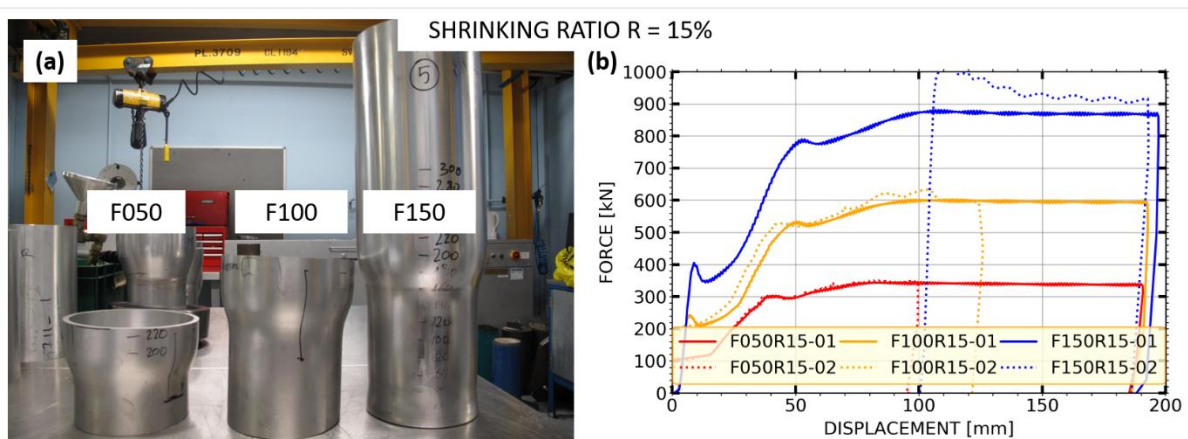


Figure 6: (a) Picture of the shrinking tubes with shrinking ratio 15% after test; (b) experimental force-displacement properties of the six specimens.

Specimens of 500 mm (-01) and 300 mm (-02) length for each of the R25 (25% shrinking ratio) tubes (F050R25, F100R25 and F150R25) were tested. Figure 7 shows the deformed shapes of a set of these tubes after test, and the force-displacement properties of the six tubes. Again, the undeformed ends of the tubes were cut and removed after testing. It should be noted that the force-displacement properties of F050R25-02 were measured after a pre-deformation stage of 80 mm of stroke. Steady-state forces of 586.3, 969.0 and 1557.4 kN were recorded for the F050R25-01, F100R25-01 and F150R25-01 samples respectively, and 600.3, 1061.8 and 1558.3 kN for the F050R25-02, F100R25-02 and F150R25-02 samples.

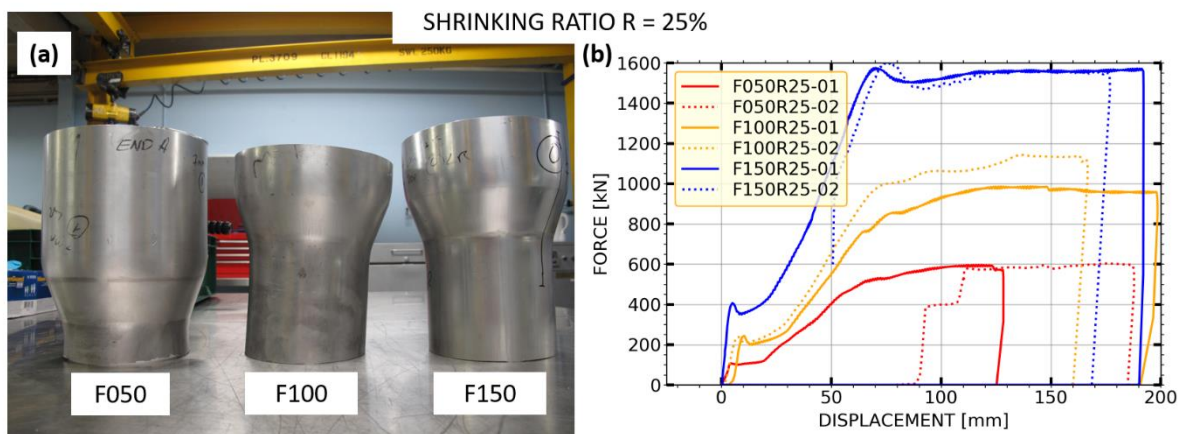


Figure 7: (a) Picture of the shrinking tubes with shrinking ratio 25% after test; (b) experimental force-displacement properties of the six specimens.

The nominal and measured shrinking ratio of the tubes are summarised in Table 3, along with the steady state forces measured during test. It can be observed that the steady state force increased as the wall thickness and/or the shrinking ratio was enlarged, although this relationship exhibited non-linear behaviour, as shown in Figure 8. Additionally, the measured deformed diameters were generally consistent for the different wall thicknesses. Two of the test configurations, F100R25 and F150R15, exhibited a larger discrepancy, with

deviations of 46.4 and 23.0 kN respectively, however, this was still within 5% of the original value.

Table 3: Tests results.

TEST SPECIMEN	LENGTH (mm)	NOMINAL SHRINKING RATIO (%)	ACTUAL SHRINKING RATIO (%)	STEADY STATE FORCE (kN)	STEADY STATE AVERAGE FORCE (kN)	STANDARD DEVIATION (kN)
F050R10 – 01	500	10	10.6	262.1	262.1	-
F100R10 – 01	500	10	10.7	514.9	514.9	-
F150R10 – 01	500	10	9.5	721.1	721.1	-
F050R15 – 01	500	15	14.9	340.1		
F050R15 – 02	300		-	345.8	342.9	2.8
F100R15 – 01	500	15	15.4	596.4		
F100R15 – 02	300		-	596.7	596.6	0.2
F150R15 – 01	500	15	15.1	868.7		
F150R15 – 02	300		-	914.7	891.7	23.0
F050R25 – 01	500	25	25.2	586.3		
F050R25 – 02	300		-	600.3	593.3	7.0
F100R25 – 01	500	25	25.9	969.0		
F100R25 – 02	300		-	1061.8	1015.4	46.4
F150R25 – 01	500	25	25.2	1557.4		
F150R25 – 02	300		-	1558.3	1557.9	0.5

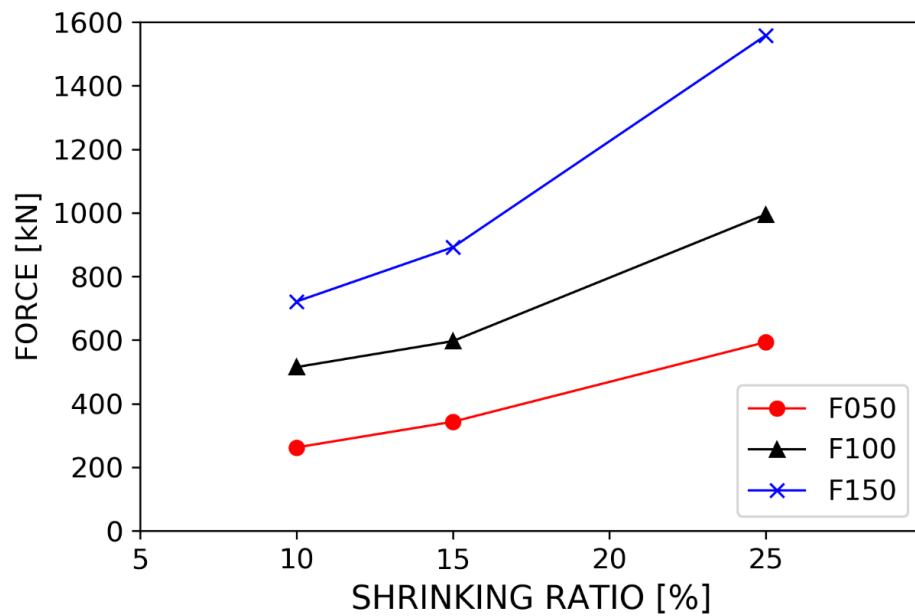


Figure 8: Steady state force vs. shrinking ratio.

3.3 Assessment of Model Parameters

The effect of the number of elements and the speed of the model have been assessed. The force-displacement properties of the axisymmetric models with the 6, 12 and 24 elements through the wall thickness of the deformation tube converged to similar values, as shown in Figure 9 (a). This indicates that the models with 6 elements through the wall thickness can be used without loss of accuracy. It is worth noting however that the properties of this model exhibited a regular pattern of peaks and troughs not observed in the other more densely discretized models. The peaks were caused by the proximity of the contacting opposite nodes of the deformation tube and die ring parts, whilst the troughs were caused by the distancing of these nodes. Greater refinement of the mesh diminished this effect without altering the average force.

The force-displacement properties for the models run at different speeds, shown in Figure 9 (b), also converged to similar values. The inertial term in the equation of motion should be negligible under quasi-static conditions, however this may become non-negligible at higher speeds. As the model run at 10 m/s displayed a more irregular force trace, indicating inertial effects taking place, it was therefore decided to run subsequent models at 1.0 m/s. In addition, the kinetic and internal-deformation energies for the models run at 1.0 m/s were compared. Figure 9 (d) shows the kinetic and internal-deformation energies for the F050R10 axisymmetric and 3D solid models. In both cases the kinetic energy amounted to approximately 0.3% of the internal energy; the ratio of kinetic energy to internal energy was similarly small for all the other models.

For a quasi-static test, there is no transition from static to dynamic friction regimes and the value of the static coefficient of friction may be regarded as a constant. Including a dynamic

coefficient of friction would lead to different mean forces between the models run at different speeds, which would invalidate the comparison. Therefore, the models discussed in Figure 9 did not include friction between the contacting parts and are only used for comparative purposes. The correlation between the experimental and numerical results, including friction, will be explored further below. Additionally, the force-displacement properties for the 2D axisymmetric and the 3D solid models with 6 elements through the wall thickness, Figure 9 (c), show the 3D solid model predicts a force 1.3% smaller than that predicted by the axisymmetric model.

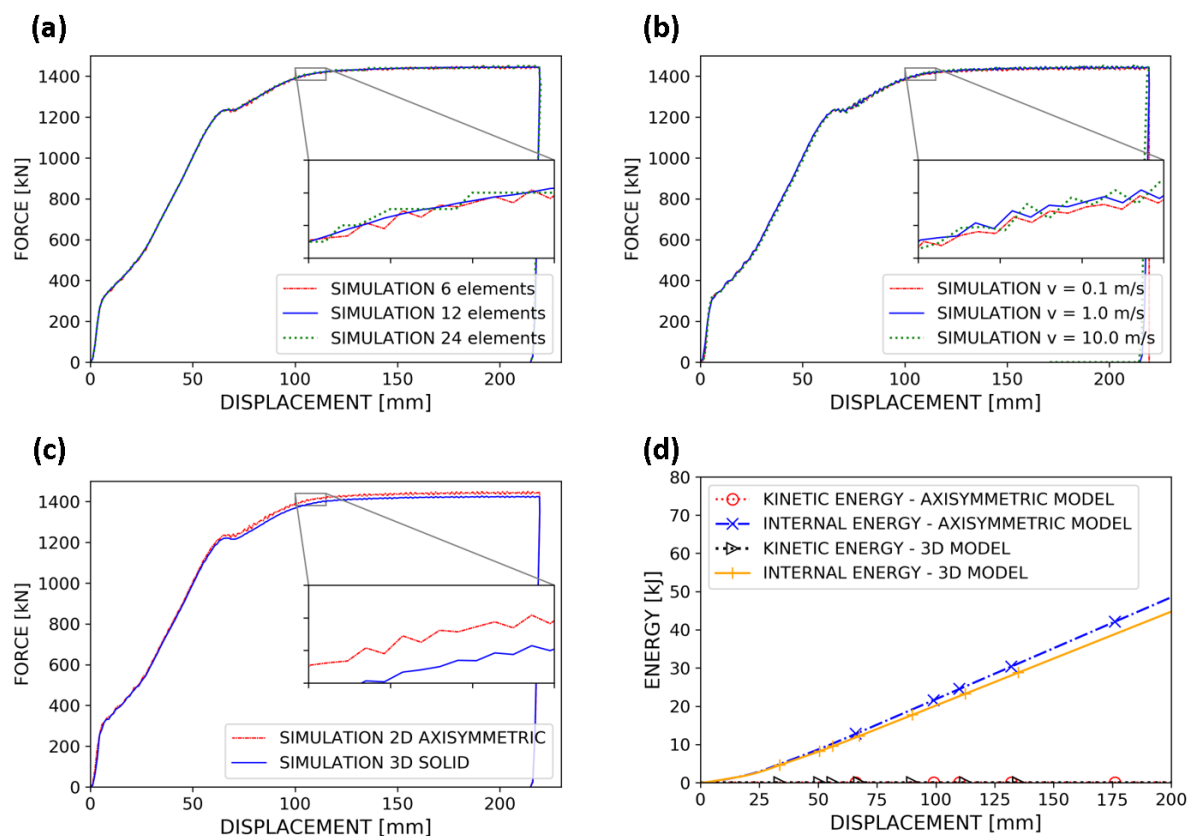


Figure 9: Force-displacement properties of the axisymmetric models with: (a) 6, 12 and 24 elements through the wall thickness of the deformation tube; (b) speed 0.1, 1.0 and 10.0 m/s (these three

models included 6 elements through thickness); (c) 2D axisymmetric and 3D solid models; and (d) kinetic and internal-deformation energies for the F050R10 axisymmetric and 3D solid models

3.4 Isotropic Numerical Modelling

Axisymmetric models were used to predict the force-displacement properties of the different tested tubes, using isotropic material models for the shrinking tubes. The thickness was modelled with 6 elements; furthermore, time scaling was employed to apply a constant speed of 1.0 m/s to the die ring and base assembly. Two numerical models were run for each sample with different friction coefficients, $\mu = 0.00$ and $\mu = 0.05$, so that the appropriate coefficient of friction could be interpolated/extrapolated from these results to match the steady state forces measured experimentally.

The force-displacement properties of the experimental and numerical results for the 10%, 15% and 25% shrinking ratio specimens are shown in Figure 10, Figure 11 and Figure 12 respectively. Generally, the numerical models were able to accurately predict the shape of the force-displacement graphs. However, the F150R25 tubes exhibited a significant peak prior to the steady-state stage, which, unlike the properties displayed by the other specimens, exceeded the magnitude of the steady state force value. The model did not account for this behaviour.

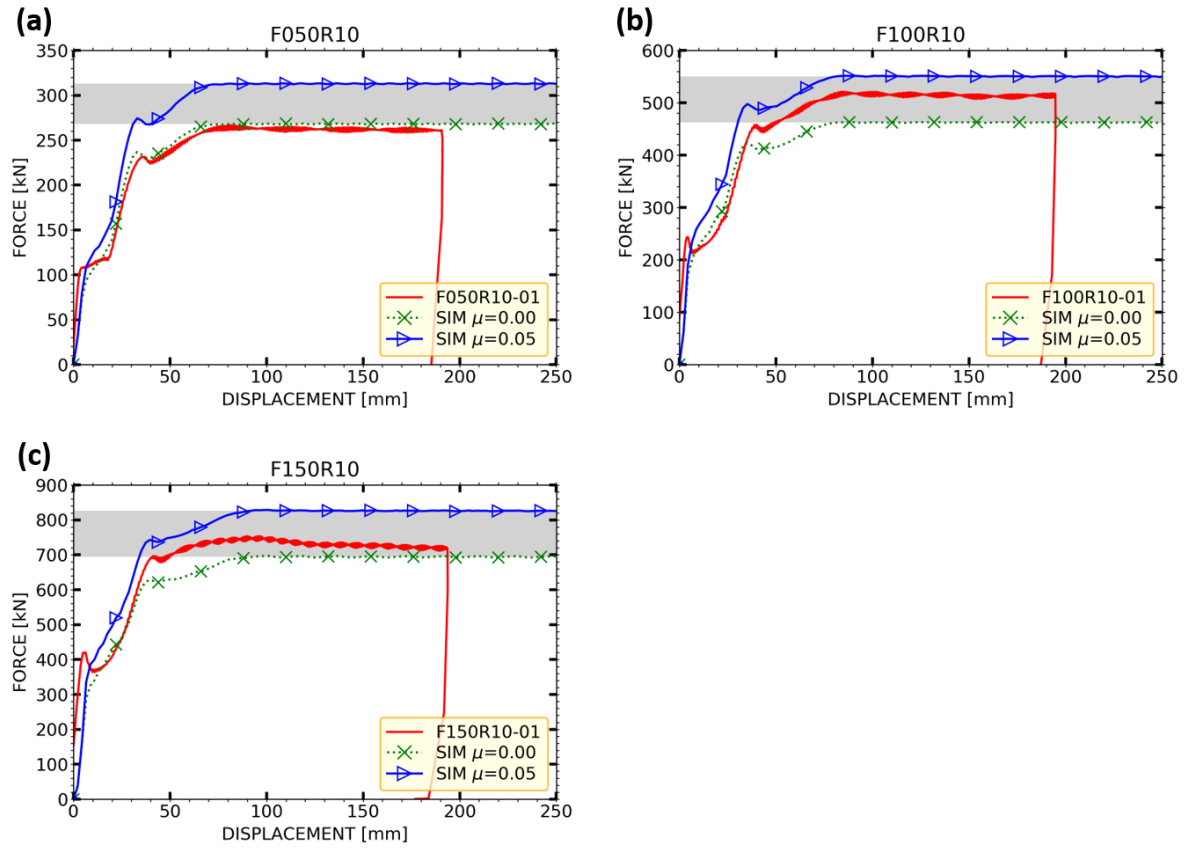


Figure 10: Comparison of force-displacement properties of the experimental and numerical results for the 10% shrinking ratio specimens (a) F050R10; (b) F100R10; and (c) F150R10.

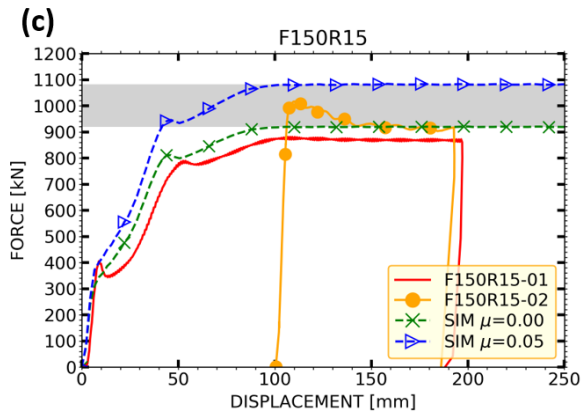
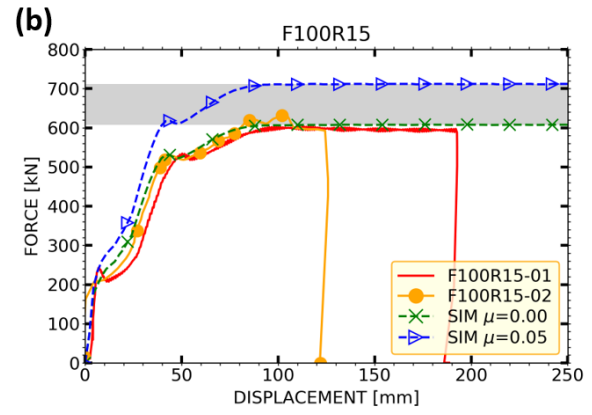
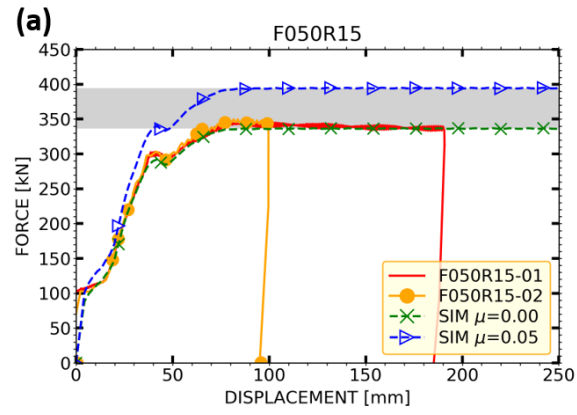


Figure 11: Comparison of force-displacement properties of the experimental and numerical results for the 15% shrinking ratio specimens (a) F050R15; (b) F100R15; and (c) F150R15.

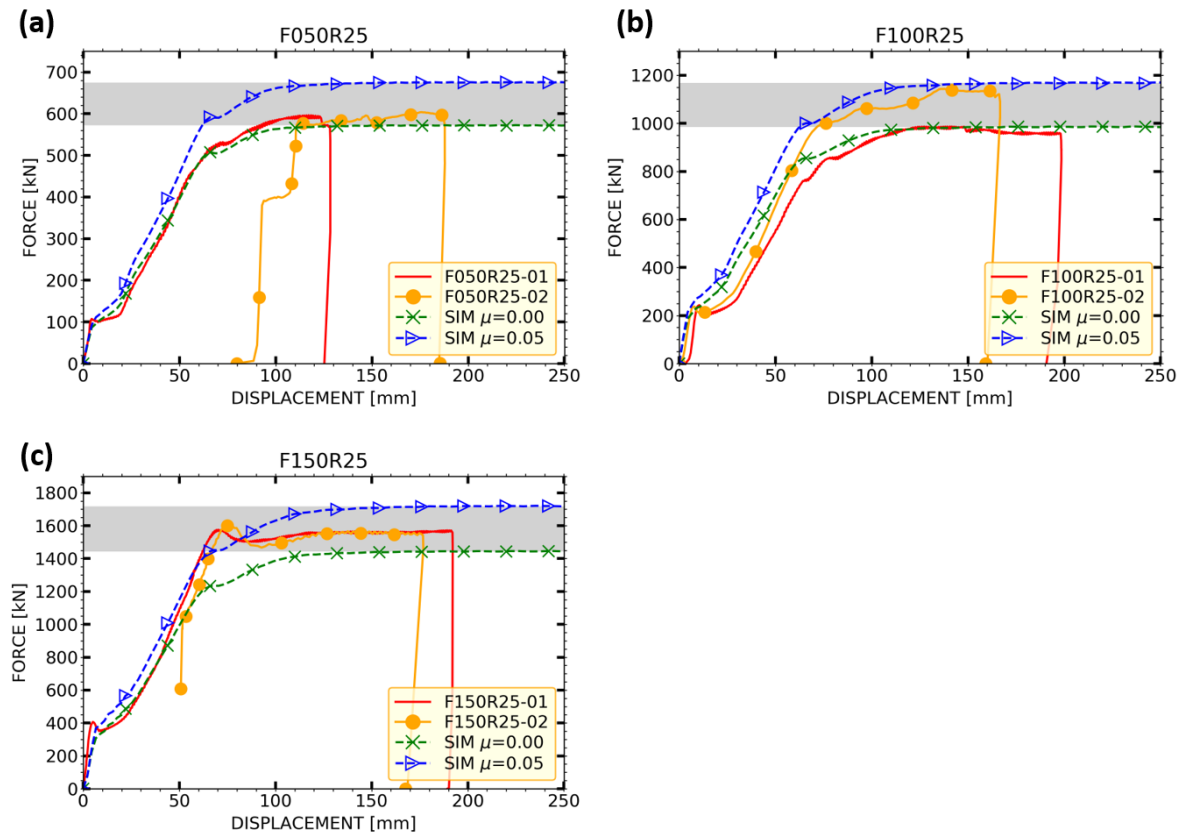


Figure 12: Comparison of force-displacement properties of the experimental and numerical results for the 25% shrinking ratio specimens: (a) F050R25; (b) F100R25; and (c) F150R25.

To understand the impact of data obtained from the transversal section of the tube, the axisymmetric F050R10, F100R10 and F150R10 numerical models were run using the stress-strain material properties found from the transversal coupon shown in Figure 4. Figure 13 shows that, as with the models that used material properties obtained from the longitudinal coupon, these models accurately depicted the shape of the force-displacement response.

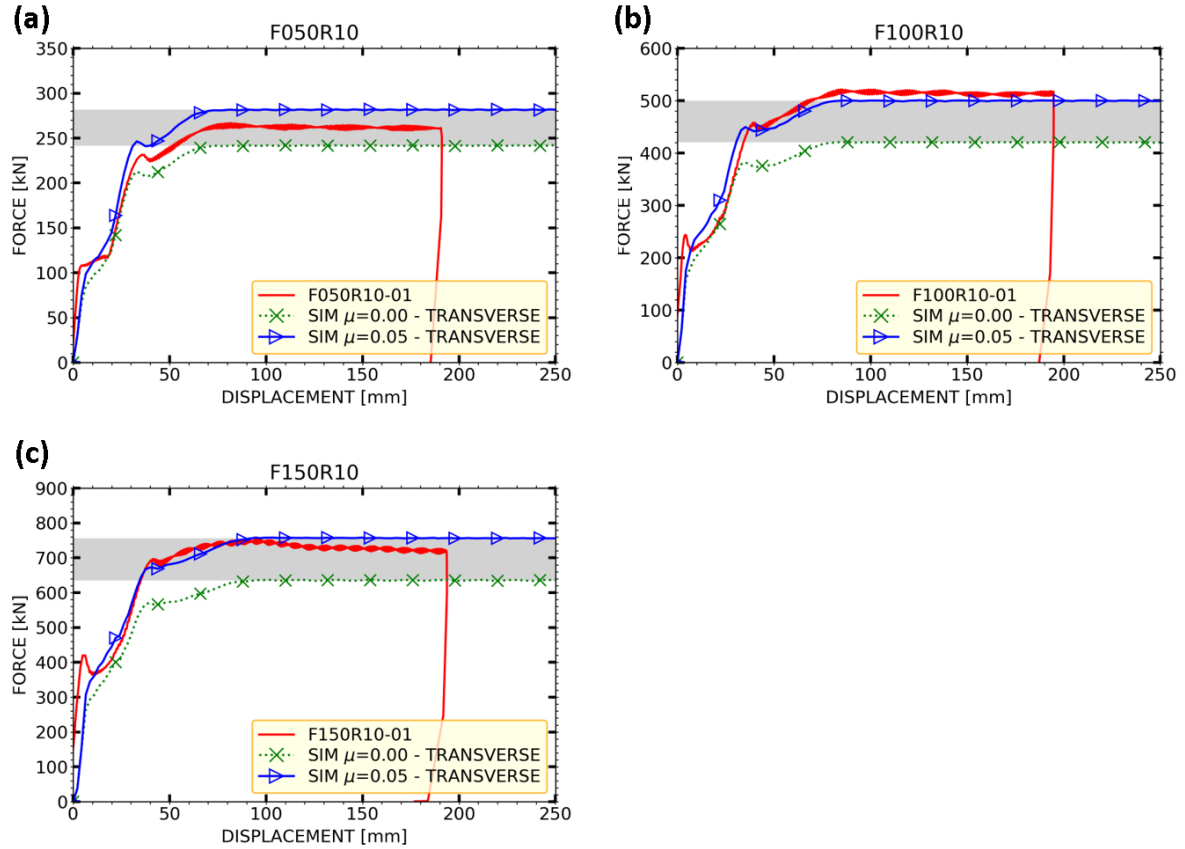


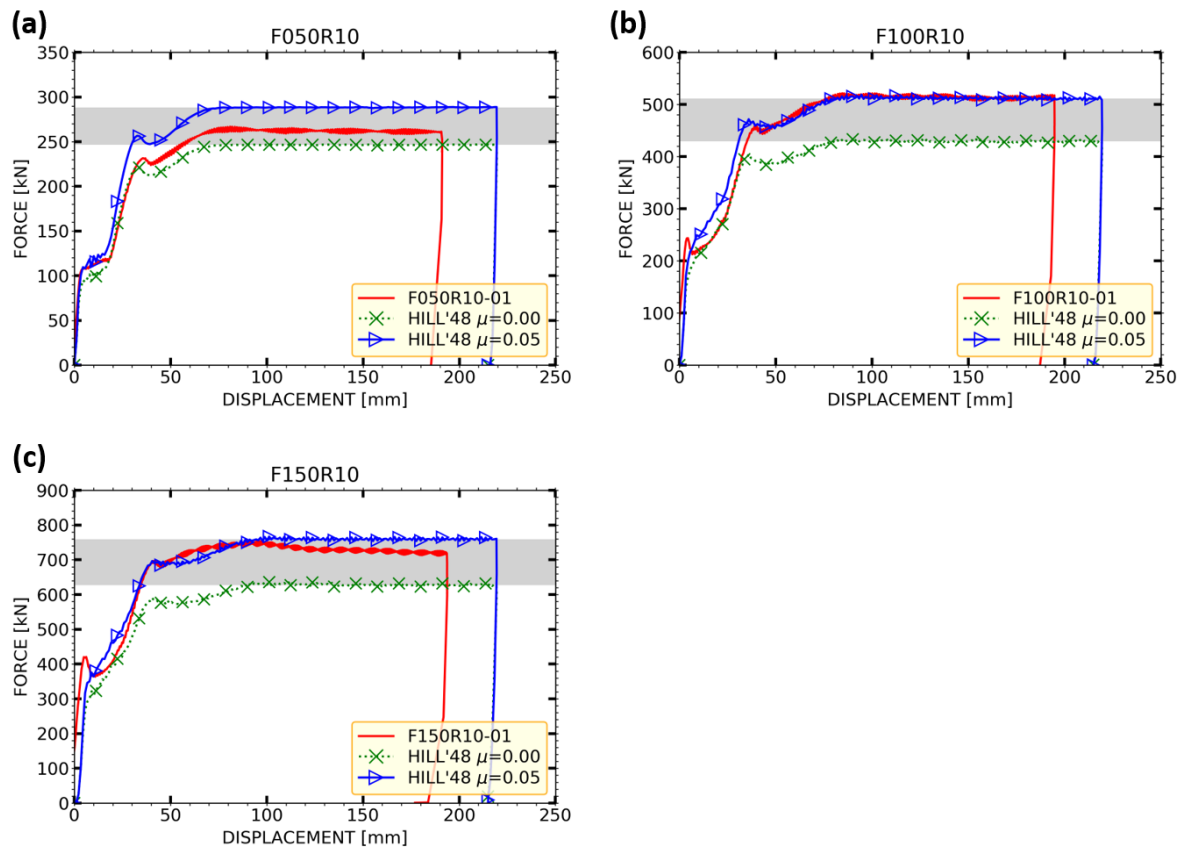
Figure 13: Comparison of force-displacement properties of the experimental and the numerical results including the material properties found from the transversal coupon; for the 10% shrinking ratio specimens (a) F050R10; (b) F100R10; and (c) F150R10.

3.5 Anisotropic Numerical Models Results

In the same manner as for the axisymmetric numerical models in the previous section, the models which included material anisotropy were run with friction coefficients of $\mu = 0.00$ and $\mu = 0.05$, so that the appropriate coefficient of friction could be interpolated/extrapolated from these results.

The comparison of the force-displacement properties of the numerical models with the Hill'48 material model and the experimental results are shown in Figure 14, Figure 15 and Figure 16 for specimens with shrinking ratios of 10%, 15% and 25% respectively.

462 It can be noted that no experimental force-displacement curve falls below the simulation
 463 predictions without friction.



464
 465 Figure 14: Force-displacement properties of the experimental and numerical results
 466 including Hill'48 material model; for the 10% shrinking ratio specimens (a) F050R10; (b)
 467 F100R10; and (c) F150R10
 468

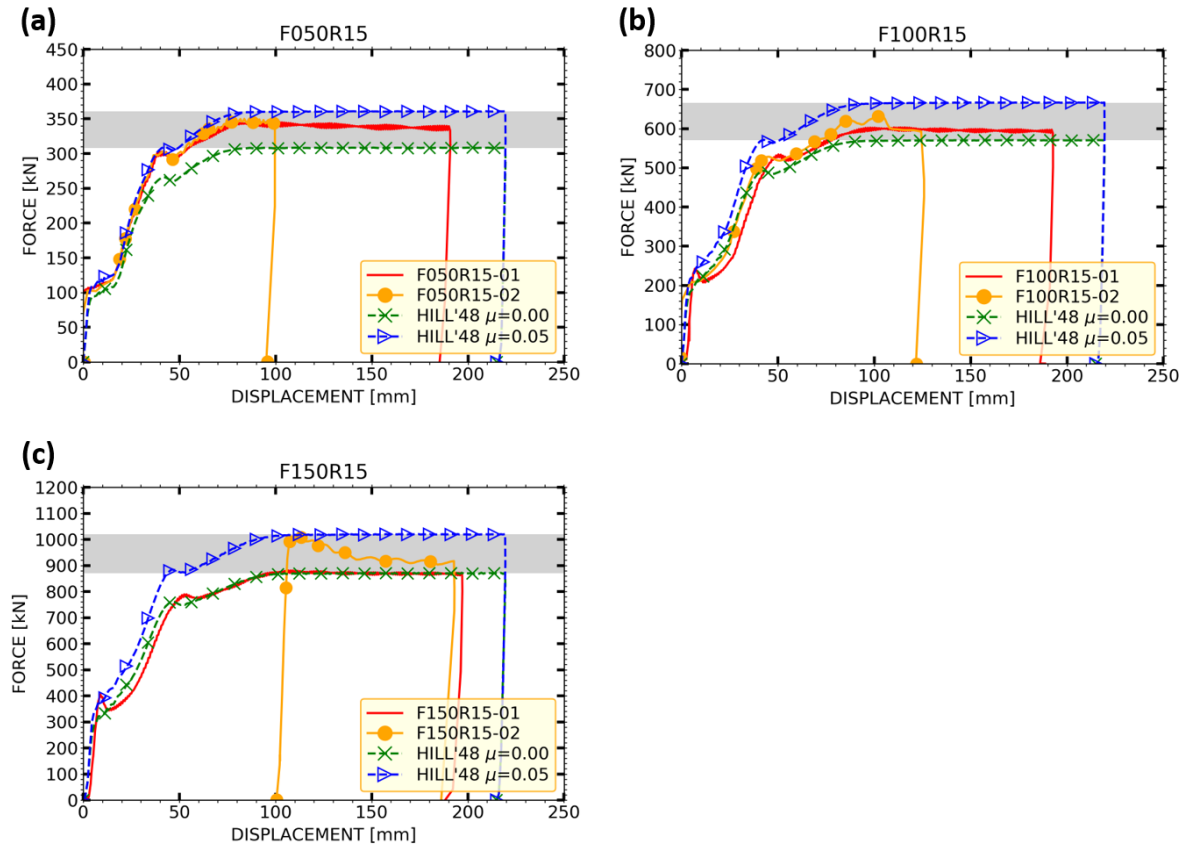


Figure 15: Force-displacement properties of the experimental and numerical results including Hill'48 material model; for the 15% shrinking ratio specimens: (a) F050R15; (b) F100R15; and (c) F150R15

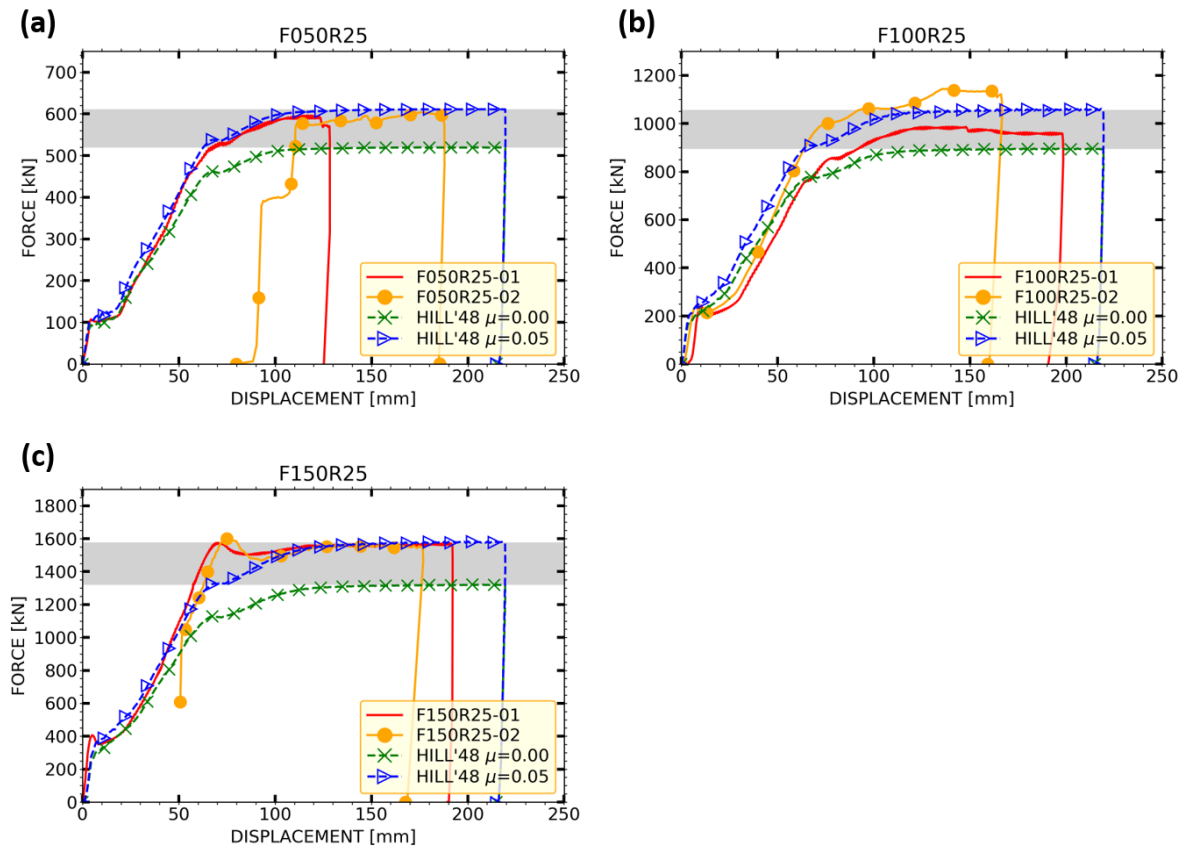


Figure 16: Force-displacement properties of the experimental and numerical results including Hill'48 material model; for the 25% shrinking ratio specimens: (a) F050R25; (b) F100R25; and (c) F150R25

4 Discussion

4.1 Shape of the Shrinking Tube

Shrinking tubes deform in a similar manner as expansion tubes. The shape of the F100R25 deformation tube, at specified intervals, together with the experimental force-displacement properties is shown in Figure 17. The deformation stages of the shrinking tube herein very closely follow those described by others [31], with this particular tube defined as large die mode [36], whereby the inner diameter of the die is larger than the critical inner diameter. In the first 5 mm of stroke, the force increases rapidly to 228 kN with the rapidity of the increase implying that this initial stage is dominated by the elastic deformation of the tube. As the stroke increases from 5 to 24 mm, the force drops slightly, before starting a gentler increase until reaching 266 kN. During this stage, the tube bends inwards as the contact point between the tube and the die slides down the conical surface of the die. The force gradient then increases until a local maximum force, of 853 kN, at a stroke of 72 mm. During this stage, the contact point between the tube and the die remains stationary, with the tube progressing further by conforming to the conical surface of the die. Beyond 72 mm of stroke, the tube reaches the transition between the conical and straight sections of the die ring, causing the tube to overshoot the die and start unbending. Thus, the force keeps increasing, albeit with a smaller gradient, until, at a stroke of 110 mm and force of 975 kN, the advancing tip of the tube finishes unbending, at which point the force is almost the steady-state force that it will exhibit thereafter.

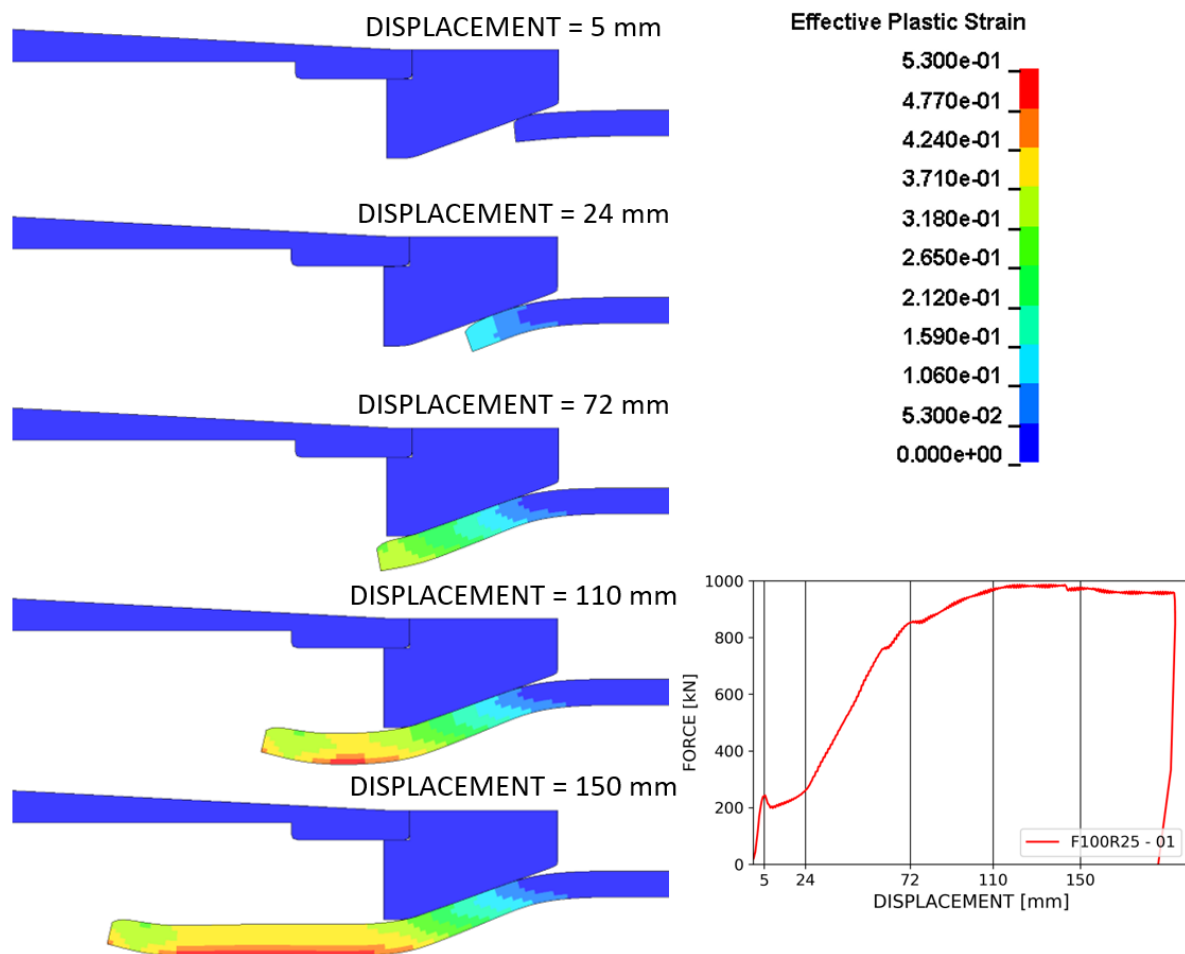


Figure 17: Evolution of the simulated F100R25 deformation tube shape, compared to the experimental force-displacement results.

4.2 Effect of Anisotropy on the Reaction Force

The results of this work suggest that: a) the reaction force of anisotropic shrinking tubes is lower than would be expected if the material was isotropic; and b) the established approach to predict the performance of energy absorbers, thus fulfilling the requirements outlined in BS EN 15227 [2], may not be appropriate when using anisotropic tubes.

Indeed, the traditional approach of predicting the expansion tubes performance by using isotropic material properties and assessing the friction coefficient from physical experiments failed in the case of three of the tested tubes herein. The models for the

512 F50R10, F100R15 and F150R15 specimens suggest that the plastic work would be sufficient
513 to exceed the reaction forces measured experimentally, even before including the effects of
514 friction. Furthermore, the predicted friction coefficients for the other six specimens were
515 much lower than was expected from the literature (as quoted in Table 1).
516 This could be expected, with the aluminium extrusions used herein demonstrating
517 anisotropic behaviour during tensile testing. Therefore, it is suggested that anisotropy may
518 be an important factor affecting the performance of shrinking tubes used as energy
519 absorbers; in this case this is manifested by a reduction in the reaction force.
520 The effect of the anisotropic properties of the aluminium extrusions on the reaction force of
521 the shrinking tubes was assessed by comparing the results of isotropic and anisotropic
522 numerical models. The material strength of the tube in the hoop direction has been shown
523 herein to be weaker than in the axial direction. As the wall of a shrinking tube is subjected
524 to large hoop strains, it could be expected that the weaker strength of the tube in the hoop
525 direction may lead to a reduced reaction force. Indeed, it has been shown that the forces
526 predicted by the anisotropic models lie between the results from axisymmetric simulations
527 using material properties from the different tube directions.
528 The steady state forces obtained experimentally and by simulation, including the isotropic
529 and anisotropic material models are summarised in Table 4. Inclusion of the Hill'48 material
530 model reduced the predicted steady state forces by 5.4-9.7% compared to the isotropic
531 numerical models. The reduction is more noticeable for the models when the shrinking ratio
532 was 25%, which may be due to the greater fraction of plastic deformation caused by the
533 larger radial shrinking ratio.
534 The predicted coefficients of friction that match the anisotropic simulation with the
535 experimental results are also detailed in Table 4. The friction coefficients range between

0.007 and 0.051, with an average value of $\mu_{ave} = 0.032$. This is still smaller than most coefficients of friction quoted in the literature, see Table 1, for shrinking and radial expansion tubes. A possible reason for this could be models employed. In particular, the inclusion of non-quadratic yield criterium has been demonstrated to improve alignment between numerical modelling and experimental test data of hydroforming of aluminium tubes [49] [50] as well as biaxial tensile and hole expansion tests [51]. Thus, using a more advanced yield criterion may lead to more accurate predictions of the reaction force of shrinking tubes.

Table 4: Summary of the steady state force experimental and simulation results, including the isotropic and Hill'48 material models, together with the predicted coefficient of friction based on the results of the numerical models with the Hill'48 material model.

SPECIMEN	AVERAGE EXPERIMENTAL STEADY STATE FORCE (kN)	SIMULATION ISOTROPIC μ = 0.00 STEADY STATE FORCE (kN)	SIMULATION HILL'48 μ = 0.00 STEADY STATE FORCE (kN)	VARIATION HILL'48/ISOTROPIC (%)	PREDICTED COEFFICIENT OF FRICTION μ (HILL'48)
F050R10	262	268	247	-8.0%	0.019
F100R10	515	463	429	-7.3%	0.051
F150R10	721	694	627	-9.7%	0.036
F050R15	343	336	308	-8.4%	0.034
F100R15	597	608	570	-6.2%	0.015
F150R15	892	919	870	-5.4%	0.007
F050R25	593	572	519	-9.2%	0.041
F100R25	1015	985	894	-9.2%	0.038
F150R25	1558	1442	1318	-8.6%	0.047

4.3 Characterization of the material

Another cause for the discrepancies between experimental data and numerical models may relate to the methodology of material characterization. The mechanical properties of the tubes in the hoop direction were determined by tensile testing of coupons extracted from the transverse direction. This methodology only enables the middle section of the coupon coinciding with the hoop direction to be evaluated as the rest of the straight length of the

coupon is partially aligned with the radial direction. As the radial alignment increases towards the shoulders of the coupons, the coupon does not solely measure the mechanical properties in the hoop direction. As such, if the material strength of the tube is greater in the radial direction than the hoop direction, the stress-strain properties in the hoop direction could be overestimated.

The Ring Hoop Tension Test (RHTT) can be used to assess the mechanical properties of tubes in the hoop direction [52]. This uses D-shaped mandrels to accommodate the curvature of the ring, and hence ensure that the sample is only subject to hoop strains. This suggests there could be significant directional differences in the properties, with the yield strength up to 20% lower in the hoop direction as opposed to longitudinally [53]. The differences observed here suggest approximately 10% difference between strengths in the hoop and longitudinal directions, and as such could affect the predicted performance slightly differently than if the difference was 20%.

5 Summary and Conclusions

To conform to the relevant standards and hence ensure suitable safety, the performance of energy absorbers for railway vehicles must be demonstrated using numerical models that have been correlated against experimental data. Traditionally, such models use isotropic material properties, however the anisotropy of the tubes may impact their performance. Thus, this paper investigated the effect of anisotropy on the performance of railway energy absorbers based on shrinking tube technology, including whether its inclusion in numerical models offered the possibility to improve accuracy.

576 The mechanical properties of AW-6082 aluminium alloy shrinking tubes were quantified,
577 with tensile tests indicating the yield strength was 10% lower in the hoop direction as
578 opposed to longitudinally.

579 Numerical models of the shrinking tubes were created with isotropic (von Mises yield
580 function) and anisotropic (Hill's quadratic yield function) material properties. The reaction
581 force was overpredicted when using isotropic material models, with values exceeding those
582 determined experimentally. As this feature prevented the numerical model from correlating
583 the test results, this does not pass the criterion defined in the standard BS EN 15227.

584 The anisotropic numerical models predicted lower reaction forces, that were correlated
585 with the test data by accounting for friction by the inclusion of a coefficient of friction of $\mu =$
586 0.03. However, this is lower than values obtained by other researchers, with two possible
587 reasons identified for this discrepancy. First, the method of material characterization is
588 likely to have overestimated the hoop yield stress by also partly accounting for the
589 longitudinal properties. Additionally, other more advanced anisotropic material models
590 have been included in other contexts that could offer greater accuracy herein. As further
591 work, it is envisaged to apply these to further improve the understanding of the effect of
592 anisotropy on energy absorbers based on shrinking tube technology. Furthermore, as the
593 energy absorbers are to be used as crash structures for railway vehicles, it is anticipated that
594 further analyses will evaluate the performance of the tubes under dynamic loading
595 conditions as opposed to quasi-static.

596

597 Acknowledgement

The authors gratefully acknowledge the financial support from Innovate UK, project reference 131817: Lightweight Energy Absorbing Aluminium Structures (LEAAST). The authors would also like to thank the participants, Constellium UK Limited, Innoval Technology Limited, Brunel University and Jaguar Land Rover Limited.

6 References

- [1 BS EN12663-1:2010, "Railway applications - Structural requirements of railway vehicle bodies. Part 1: Locomotives and passenger rolling stock (and alternative method for freight wagons)," 2010.
- [2 BS EN 15227:2008+A1:2010, "Railway applications - Crashworthiness requirements for railway vehicle bodies," 2010.
- [3 J. Alexander, "An approximate analysis of the collapse of thin cylindrical shells under axial loading," *Quart. Journ. Mech. and Applied Math*, vol. 13, 1960.
- [4 A. Starlinger, "On the application of ABAQUS for the evaluation of the structural integrity of railway vehicles," in *SIMULIA Customer Conference*, Barcelona, 2011.
- [5 M. Pereira, P. Barros and P. Jumin, "Passive safety concepts for periurban trams," in *Passive Safety of Rail Vehicles - 4th International Symposium*, Berlin, 2003.
- [6 M. Seitzberger, A. Rittenschober and H. Payer, "A simple design approach for the stabilization of anticlimbing devices for attached deformation elements in offset collisions of trains," in *Passive Safety of Rail Vehicles - 5th International Symposium*, Berlin, 2005.
- [7 A. Baroutaji, M. Sajjia and A. Olabi, "On the crashworthiness performance of thin-walled energy absorbers: Recent advances and future developments," *Thin-Walled Structures*, vol. 118, pp. 137-163, 2017.

- [8] C. Calladine and R. English, "Strain rate and inertia effects in the collapse of two types of energy-absorbing structure," *International Journal of Mechanical Sciences*, vol. 26, pp. 689-701, 1984.
- [9] W. Stronge, T. Yu and W. Johnson, "Long stroke energy dissipation in splitting tubes," *International Journal of Mechanical Sciences*, vol. 25, pp. 637-647, 1983.
- [1] S. Schneider, "The EST Crash Buffer," EST Eisenbahn-Systemtechnik GmbH, 2020. [Online]. Available: <http://www.crashbuffer.com/>. [Accessed 5 10 2020].
- [1] J. Magliaro and W. Altenhof, "Mechanical performance and crashworthiness of plates and extrusions subjected to cutting: An overview," *Thin-Walled Structures*, vol. 148, 2020.
- [1] Y. Peng, S. Wang, S. Yao and P. Xu, "Crashworthiness analysis and optimization of a cutting-style energy absorbing structure for subway vehicles," *Thin-Walled Structures*, vol. 120, pp. 225-235, 2017.
- [1] G. Gao, W. Guan, J. Li, H. Dong, X. Zou and W. Chen, "Experimental investigation of an active-passive integration energy absorber for railway vehicles," *Thin-Walled Structures*, vol. 117, pp. 89-97, 2017.
- [1] Axtone, "Axtone scientific know-how," Axtone, [Online]. Available: <http://axtoneglobal.com/know-how/>. [Accessed 5 10 2020].
- [1] Voith, "Energy absorption elements," Voith, [Online]. Available: <http://voith.com/uk-en/products-services/connection-components-couplings/railway-couplers-connections/energy-absorption-elements.html?130395%5B%5D=1>. [Accessed 9 10 2020].
- [1] Dellner, "Crash energy management," Dellner, [Online]. Available: <https://www.dellner.com/SitePages/ProductGallery.aspx?application=All&location=All&product=Crash%20Energy%20Management&types=>. [Accessed 9 10 2020].
- [1] Oleo International, "Rail," Oleo International, [Online]. Available: <https://www.oleo.co.uk/products/rail>. [Accessed 9 10 2020].
- [1] T. Daxner, F. Rammerstorfer and F. Fischer, "Instability phenomena during the conical expansion of circular cylindrical shells," *Computer Methods in Applied Mechanics and Engineering*, vol. 194, no. 21-24, pp. 2591-2603, 2005.
- [1] F. Fischer, F. Rammerstorfer and T. Daxner, "Flaring—An analytical approach," *International Journal of Mechanical Sciences*, vol. 48, no. 11, pp. 1246-1255, 2006.
- [2] B. Almeida, M. Alves, P. Rosa, A. Brito and P. Martins, "Expansion and reduction of thin-walled tubes using a die: experimental and theoretical investigation," *International Journal of Machine Tools and Manufacture*, vol. 46, pp. 1643-1652, 2006.

- [2 A. Karrech and A. Seibi, "Analytical model for the expansion of tubes under tension," *Journal of Materials Processing Technology*, vol. 210, no. 2, pp. 356-362, 2010.
- [2 O. Al-Abri and T. Pervez, "Structural behavior of solid expandable tubular undergoes radial expansion process – Analytical, numerical, and experimental approaches," *International Journal of Solids and Structures*, vol. 50, no. 19, pp. 2980-2994, 2013.
- [2 Y. Liu and X. Qiu, "A theoretical study of the expansion metal tubes," *International Journal of Mechanical Sciences*, vol. 114, pp. 157-165, 2016.
- [2 Y. Liu, X. Qiu, W. Wang and T. Yu, "An improved two-arcs deformational theoretical model of the expansion tubes," *International Journal of Mechanical Sciences*, vol. 133, pp. 240-250, 2017.
- [2 J. Zhu, T. Wierzbicki, K. Pack and S. Roggeband, "Characterization of the cyclic loading in the tube expansion process," *International Journal of Mechanical Sciences*, vol. 150, pp. 112-126, 2019.
- [2 G. Centeno, M. Silva, L. Alves, C. Vallellano and P. Martins, "On the Utilization of Circle Grid Analysis in Thin-walled Forming of Tubes: Experimental and Numerical Evaluation," *Procedia Engineering*, vol. 207, pp. 1773-1778, 2017.
- [2 G. Centeno, M. Silva, L. Alves, C. Vallellano and P. Martins, "Towards the characterization of fracture in thin-walled tube forming," *International Journal of Mechanical Sciences*, vol. 119, pp. 12-22, 2016.
- [2 J. Magrinho, G. Centeno, M. Silva, P. Vallellano and P. Martins, "On the formability limits of thin-walled tube inversion using different die fillet radii," *Thin-Walled Structures*, vol. 144, pp. 0263-8231, 2019.
- [2 M. Shakeri, S. Salehghaffari and R. Mirzaeifar, "Expansion of circular tubes by rigid tube as impact energy absorbers: experimental and theoretical investigation," *International Journal of Crashworthiness*, vol. 12, pp. 493-501, 2007.
- [3 J. Yan, S. Yao, P. Xu, Y. Peng, H. Shao and S. Zhao, "Theoretical prediction and numerical studies of expanding circular tubes as energy absorbers," *International Journal of Mechanical Sciences*, vol. 105, pp. 206-214, 2016.
- [3 J. Yang, M. Luo, Y. Hua and G. Lu, "Energy absorption of expansion tubes using a conical-cylindrical die: Experiments and numerical simulation," *International Journal of Mechanical Sciences*, vol. 52, no. 5, pp. 716-725, 2010.
- [3 M. Luo, J. Yang, H. Liu, G. Lu and J. Yu, "Energy absorption of expansion tubes using a conical-cylindrical die: Theoretical model," *International Journal of Mechanical Sciences*, vol. 157-158, pp. 207-220, 2019.

- [3 K. Ahn, J. Kim and H. Huh, "The effects of local buckling on the crash energy absorption of
3] thin-walled expansion tubes," in *Numisheet 2008*, Interlaken, Switzerland, 2008.
- [3 S. Yao, Z. Li, J. Yan, P. Xu and Y. Peng, "Analysis and parameters optimization of an
4] expanding energy-absorbing structure for a rail vehicle coupler," *Thin-Walled Structures*,
vol. 125, pp. 129-139, 2018.
- [3 J. Li, G. Gao, W. Guan, S. Wang and Y. Yu, "Experimental and numerical investigations on the
5] energy absorption of shrink circular tube under quasi-static loading," *International Journal
of Mechanical Sciences*, vol. 137, pp. 284-294, 2018.
- [3 Y. Liu and X. Qiu, "A theoretical model of the shrinking metal tubes," *International Journal of
6] Mechanical Sciences*, vol. 144, pp. 564-575, 2018.
- [3 S. Yao, Z. Li, W. Ma and P. Xu, "Crashworthiness analysis of a straight-tapered shrink tube,"
7] *International Journal of Mechanical Sciences*, vol. 157-158, pp. 512-527, 2019.
- [3 J. Tanaskovic, D. Milkovic, V. Lucanin and G. Vasic Franklin, "Experimental investigations of
8] the shrinking-splitting tube collision energy absorber," *Thin-walled Structures*, vol. 86, pp.
142-147, 2015.
- [3 C. Moreno, S. Reid and T. Williams, "Experimental and numerical assessment of oblique
9] loading quasi-static testing of railway anticlimbers," *Proceedings of the Institution of
Mechanical Engineers, Part F: Journal of Rail and Rapid Transit*.
- [4 Y. Korkolis and S. Kyriakides, "Inflation and burst of anisotropic aluminum tubes for
0] hydroforming applications," *International Journal of Plasticity*, vol. 24, pp. 509-543, 2008.
- [4 Y. Korkolis and S. Kyriakides, "Inflation and burst of aluminum tubes. Part II: An advanced
1] yield function including deformation-induced anisotropy," *International Journal of
Plasticity*, vol. 24, no. 9, pp. 1625-1637, 2008.
- [4 L. Belhassen, S. Koubaa, M. Wali and F. Dammak, "Anisotropic effects in the compression
2] beading of aluminum thin-walled tubes with rubber," *Thin-Walled Structures*, vol. 119, pp.
902-910, 2017.
- [4 J. Magrinho, M. Silva, G. Centeno, F. Moedas, C. Vallellano and P. Martins, "On the
3] determination of forming limits in thin-walled tubes," *International Journal of Mechanical
Sciences*, vol. 155, pp. 381-391, 2019.
- [4 BS EN 573-3:2007, "Aluminium and aluminium alloys - Chemical composition and form of
4] wrought products - Part 3: Chemical composition and form of products," BSI.
- [4 BS EN 6892-1:2009, "Metallic materials - Tensile testing - Part 1: Method of test at ambient
5] temperature," BSI.

- [4 R. Hill, The mathematical theory of plasticity, Oxford: Oxford University Press, 1950.
6]
- [4 D. Banabic, Sheet metal forming processes : constitutive modelling and numerical
7] simulation, Berlin: Springer, 2010.
- [4 J. Hallquist, LS-Dyna theory manual, Livermore Software Technology Corporations, 2006.
8]
- [4 Y. Korkolis and S. Kyriakides, "Hydroforming of anisotropic aluminum tubes: Part I
9] experiments," *International Journal of Mechanical Sciences*, vol. 53, no. 2, pp. 75-82, 2011.
- [5 Y. Korkolis and S. Kyriakides, "Hydroforming of anisotropic aluminum tubes: Part II
0] analysis," *International Journal of Mechanical Sciences*, vol. 53, no. 2, pp. 83-90, 2011.
- [5 T. Kuwabara, K. Hashimoto, E. Iizuka and J. Yoon, "Effect of anisotropic yield functions on
1] the accuracy of hole expansion simulations," *Journal of Materials Processing Technology*, vol.
211, no. 3, pp. 475-481, 2011.
- [5 C. Dick and Y. Korkolis, "Mechanics and full-field deformation study of the Ring Hoop
2] Tension Test," *International Journal of Solids and Structures*, vol. 51, no. 18, pp. 3042-3057,
2014.
- [5 C. Dick and Y. Korkolis, "Anisotropy of thin-walled tubes by a new method of combined
3] tension and shear loading," *International Journal of Plasticity*, vol. 71, pp. 87-112, 2015.

611
612
613
614